Evolution of electronic and magnetic properties in a series of iridate double perovskites $Pr_{2-x}Sr_xMgIrO_6$ ($x = 0, 0.5, 1.0$)

Abhisek Bandyopadhyay,[1,*] Ilaria Carlomagno,[2] Laura Simonelli,[3] M. Moretti Sala,[4,5] A. Efimenko,[4] Carlo Meneghini,[2] and Sugata Ray[1]

[1]*School of Materials Science, Indian Association for the Cultivation of Science, 2A and 2B Raja S. C. Mullick Road, Jadavpur, Kolkata 700 032, India*

[2]*Dipartimento di Scienze, Universitá Roma Tre, Via della Vasca Navale, 84 I-00146 Roma, Italy*

[3]*BL22–CLÆSS: Core Level Absorption and Emission Spectroscopies Beamline–Experiments Division, ALBA Synchrotron Light Source, Ctra. BP 1413 km. 3,3 08290 Cerdanyola del Vallès, Barcelona, Spain*

[4]*ESRF–The European Synchrotron, 71 Avenue des Martyrs, 38000 Grenoble, France*

[5]*Dipartimento di Fisica, Politecnico di Milano, P.zza Leonardo da Vinci 32, I-20133 Milano, Italy*

(Received 20 June 2019; revised manuscript received 6 August 2019; published 22 August 2019)

Spin-orbit coupling (SOC) plays a crucial role in magnetic and electronic properties of 5*d* iridates. In this paper we have experimentally investigated the structural and physical properties of a series of Ir-based double perovskite compounds $Pr_{2-x}Sr_xMgIrO_6$ ($x = 0, 0.5, 1$; hereafter abbreviated as PMIO, PSMIO1505, and PSMIO). Interestingly, these compounds have recently been proposed to undergo a transition from the spin-orbit-coupled Mott insulating phase at $x = 0$ to the elusive half-metallic antiferromagnetic (HMAFM) state with Sr doping at $x = 1$. However, our detailed magnetic and electrical measurements refute any kind of HMAFM possibility in either of the doped samples. In addition, we establish that within these $Pr_{2-x}Sr_xMgIrO_6$ double perovskites, changes in Ir-oxidation states (4+ for PMIO to 5+ for PSMIO via mixed 4+/5+ for PSMIO1505) lead to markedly different magnetic behaviors. While SOC on Ir is at the root of the observed insulating behaviors for all three samples, the correlated magnetic properties of these three compounds develop entirely due to the contribution from local Ir moments. Additionally, the magnetic Pr^{3+} ($4f^2$) ions, instead of showing any kind of ordering, only contribute to the total paramagnetic moment. It is seen that the $PrSrMgIrO_6$ sample does not order down to 2 K despite antiferromagnetic interactions. But, the d^5 iridate Pr_2MgIrO_6 shows a sharp antiferromagnetic (AFM) transition at around 14 K, and in the mixed valent $Pr_{1.5}Sr_{0.5}MgIrO_6$ sample the AFM transition is shifted to a much lower temperature (~6 K) due to weakening of the AFM exchange.

DOI: 10.1103/PhysRevB.100.064416

I. INTRODUCTION

In contrast to the traditional wisdom of achieving uncorrelated wide band metals in 5*d* iridates, spin-orbit coupling (SOC) plays a pivotal role in defining their complex magnetic and electronic ground states [1]. Due to a delicate balance between SOC (λ_0), Coulomb correlation (U), and crystal field energy (Δ_{CFE}), 5*d* iridates particularly offer a promising avenue for hosting diverse physical properties [2]. Strong SOC has been identified as the electronic reason for setting up an insulating band gap in Sr_2IrO_4 and other tetravalent iridates [1–5]. On the other hand, the relatively less explored pentavalent iridates (Ir^{5+}: $5d^4$) stirred up a controversy about the origin of magnetism in them. Large SOC in low-spin Ir^{5+} produces 15 possible organizations of spin-orbit-coupled J states (four electrons in three degenerate t_{2g} orbitals each having two spin arrangements), with the atomic $J = 0$ as the lowest energy state [6,7], as shown in Figs. 1(a)–1(c). But surprisingly, a pure nonmagnetic $J = 0$ state has never been realized in any of the reported d^4 Ir compounds to date [7–10]. Actually the strength of SOC and Hund's exchange together determine the relative stability of the LS/jj coupled multiplet states [Fig. 1(b)]. One plausible route for magnetic moment generation in these d^4 iridates has been assigned to Van Vleck–type intrasite singlet-triplet excitations ($J = 0 \rightarrow J = 1$) due to comparable energy scales between superexchange (mediated by complex Ir-O–O-Ir paths) and SOC-driven singlet-triplet gap [11]. Otherwise, another most prominent factor against the observation of a nonmagnetic state could be the solid state effects, such as large bandwidth of the 5*d* orbitals, ligand-Ir charge transfer, noncubic crystal field, and intersite Ir-Ir hopping which always act against the atomic SOC effect [8,11–13], and hence, produce finite magnetic moments [7,10,14]. In fact, there is an active debate running currently regarding the trueness of the proposal of excitonic magnetism in these cases against the ground state magnetism, originated by hopping and other solid state effects [15].

In this backdrop, a recent theoretical claim of half-metallic antiferromagnetism (HMAFM) appeared for a d^4 iridate double perovskite (DP) compound $PrSrMgIrO_6$ [16]. The half-metallicity (HM) has been proposed by first assuming the dominance of exchange splitting which prevents the mixing of spin-up and spin-down bands and ensures 100% spin

*Corresponding author: msab3@iacs.res.in, abhisek.ban2011@gmail.com

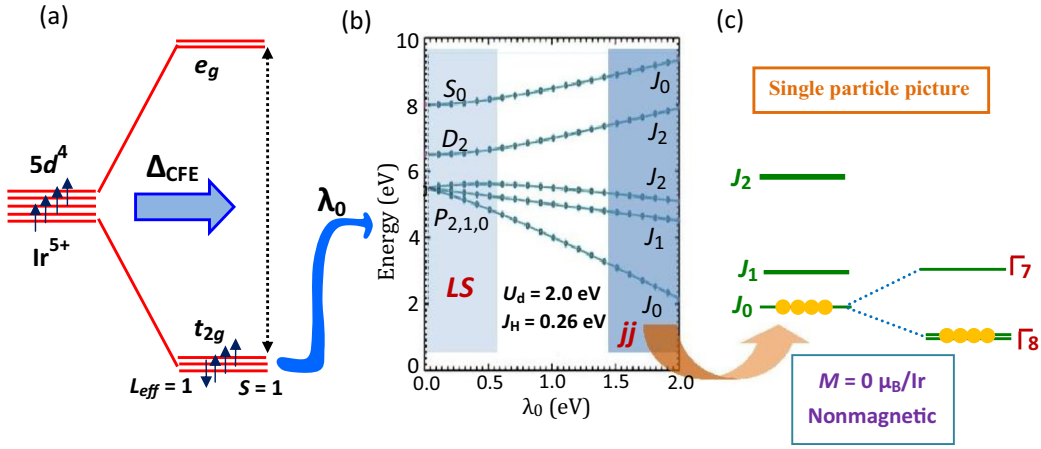

FIG. 1. Redistribution of d^4 orbitals of an Ir^{5+} ion under octahedral crystal field (a), then atomic SOC (b) to form spin-orbit-coupled multiplet states, and finally a nonmagnetic $J = 0$ state under strong SOC limit (c) in the single- particle picture.

polarization at Fermi energy E_F. Hence the strength of the SOC has been considered to be comparatively negligible and Ir energy levels have been treated within *LS* coupling limit. On the other hand, the vanishing net macroscopic magnetic moment has been described by antiferromagnetic (AFM) coupling of Pr^{3+} ($4f^2$: 2 μ_B) with the Ir^{5+} ($5d^4$) moment in the *LS* coupling limit. On the other hand, the undoped double perovskite Pr_2MgIrO_6 is predicted to be a ferrimagnetic Mott insulator [16,17]. Clearly, a few controversies prevailed with this description, such as the following: (i) despite having strong SOC on Ir^{5+}, prediction of half-metallicity in the two Sr-doped compounds and development of the large magnetic moment/Ir^{5+} ion in the $PrSrMgIrO_6$ compound, and (ii) unlike the other existing perovskite/double perovskite compounds, the non-Kramer Pr^{3+} ion at the *A* site of the present set of double perovskites is predicted to be exchange coupled to the magnetic *B* site to provide the magnetic ground state. Thus, in order to sort out the aforementioned contradictions, we have synthesized the Ir-based DP compounds $Pr_{2-x}Sr_xMgIrO_6$ ($x = 0, 0.5, 1$; hereafter identified as PMIO, PSMIO1505, and PSMIO) to verify the magnetic and electronic properties of them. Interestingly, subtle differences in the IrO_6 octahedral distortions, and also changes in the Ir-valence state upon Sr doping show a profound influence on their physical properties.

Here in this paper we show that, neither half-metallicity nor any kind of long-range AFM/ferrimagnetic ordering is observed in either of the doped compounds. Finally, our experimental observations reveal the actual scenario: Pr^{3+} does not undergo any kind of magnetic ordering or spin freezing down to the lowest measuring temperature in all these compounds; instead, the Pr^{3+} only contributes to the total paramagnetic moment. Like in other Ir-based oxides [8,10,18,19], the ground state magnetic properties of these compounds are solely influenced by the spin-orbit-coupled *J* states of Ir. In $PrSrMgIrO_6$ (PSMIO), featureless magnetic susceptibility, AFM interactions, and no sign of magnetic ordering down to 2 K are evident. Further, the presence of a small magnetic moment at the Ir site drives this system away from the ideal $J = 0$ limit. On the other hand, the undoped Pr_2MgIrO_6 (PMIO) (Ir^{4+}: $5d^5$, magnetic species) undergoes a long-range AFM transition at around 14 K. In the mixed valent $Pr_{1.5}Sr_{0.5}MgIrO_6$ (PSMIO1505) compound, the AFM transition gets weakened with the introduction of Ir^{5+}. On top of such magnetizations, all three compounds exhibit SOC-driven insulating ground states.

II. EXPERIMENTAL SECTION

Polycrystalline $Pr_{2-x}Sr_xMgIrO_6$ ($x = 0, 0.5, 1$) samples have been synthesized by the conventional solid state reaction technique. Stoichiometric amounts of high purity (>99.9%) Pr_2O_3, $SrCO_3$, MgO, and IrO_2 powders were thoroughly mixed in an agate mortar. This mixture has been calcined initially at 850 °C for 12 h in air to decompose carbonates and finally sintered at 1250 °C for 48 h in air with few intermediate grindings. The structural characterization of all the samples was performed using a Bruker AXS: D8 Advance x-ray diffractometer. The x-ray-diffraction (XRD) data were analyzed by using the Rietveld technique and refinements were done using the FULLPROF program [20]. To verify homogeneity and any off-stoichiometry in the sample, energy dispersive x-ray (EDX) analysis was also performed using a field emission scanning electron microscope (JEOL, JSM-7500F). Electrical resistivity was measured by a standard four-probe method within a temperature range of 200–400 K in a laboratory-based resistivity setup. Magnetization measurements in the temperature range 2–300 K and in magnetic fields up to ±5 T were performed in a superconducting quantum interference device (SQUID) magnetometer (Quantum Design). Ir L_3-edge x-ray absorption fine-structure (XAFS) experiments of the respective samples have been performed at the BL22-CLÆSS beamline of ALBA (Barcelona, Spain) [21] synchrotron radiation facility at room temperature in standard transmission geometry. Data treatment and quantitative analysis of EXAFS (extended x-ray absorption fine structure) were carried out using the freely available DEMETER package [22,23] (Athena and Artemis programs) using atomic clusters from crystallographic structure to (i) individuate the single and multiple scattering contributions relevant for the quantitative EXAFS data refinement and (ii) calculate (FEFF6L program) the theoretical

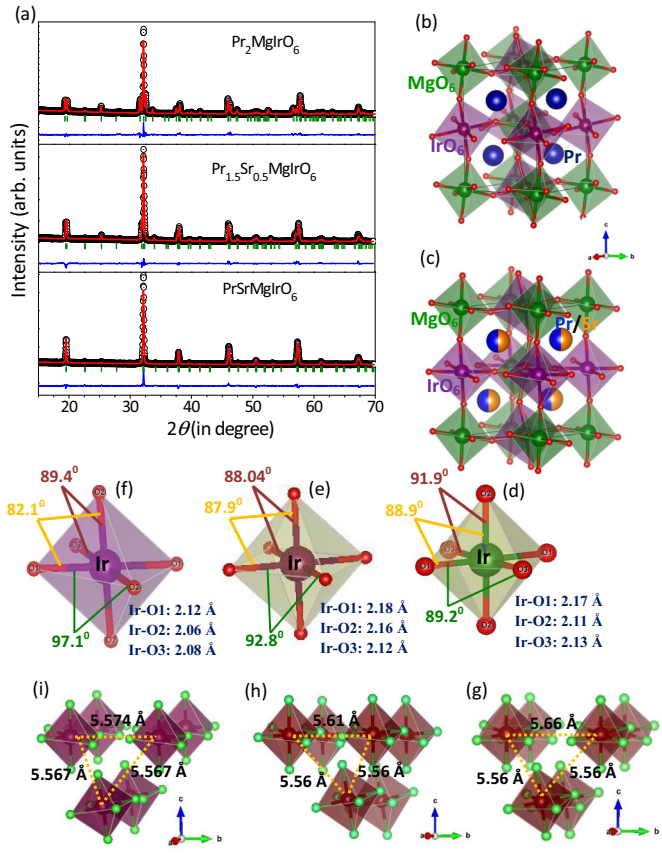

FIG. 2. (a) Rietveld refined XRD patterns of all the synthesized samples. Open black circles represent the experimental data and the continuous red line represents the calculated pattern. The blue line represents the difference between the observed and calculated patterns while the vertical green lines indicate the Bragg position for all the samples. The refined crystal structures for (b) Pr_2MgIrO_6 and (c) $PrSrMgIrO_6$. The rotational distortions (change in O-Ir-O bond angles) within the IrO_6 octahedral unit for Pr_2MgIrO_6 (d), $Pr_{1.5}Sr_{0.5}MgIrO_6$ (e), and $PrSrMgIrO_6$ (f) samples. In addition, the extent of the geometric frustration caused by Ir triangles is shown for the Pr_2MgIrO_6 (g), $Pr_{1.5}Sr_{0.5}MgIrO_6$ (h), and $PrSrMgIrO_6$ (i) compounds.

amplitude and phase functions required to calculate the theoretical EXAFS curve assuming Gaussian disorder. The x-ray photoemission spectroscopy (XPS) measurements were carried out using an Omicron electron spectrometer, equipped with a Scienta omicron sphera analyzer and Al $K\alpha$ monochromatic source with an energy resolution of 0.5 eV. Before collecting the spectra the sample surface was sputtered with argon ion bombardment for each of these samples to remove any kind of surface oxidization effect and the presence of environmental carbons in the pelletized samples. The collected spectra were processed and analyzed with the KOLXPD program. Further, the RIXS (resonant inelastic x-ray scattering) measurements at the Ir L_3 edge of the $PrSrMgIrO_6$ sample were performed at the ID20 beamline of the European Synchrotron Radiation Facility (ESRF) using π-polarized photons and a scattering geometry with $2\theta \simeq 90^\circ$ to suppress elastic scattering. A spherical, diced Si(844) analyzer was used in a Rowland circle of 2 m radius in combination with a custom-built hybrid pixel detector, having an overall energy resolution of ≈29 meV at the Ir L_3 edge in this configuration. Apart, Ir L_3-RIXS of Pr_2MgIrO_6 and $Pr_{1.5}Sr_{0.5}MgIrO_6$ samples was measured at the CLEAR spectrometer of the BL22-CLÆSS beamline of the ALBA synchrotron radiation facility with an energy resolution ≈1 eV.

III. RESULTS AND DISCUSSION

A. Structure from x-ray diffraction

Rietveld refined powder XRD patterns, obtained from polycrystalline samples of $Pr_{2-x}Sr_xMgIrO_6$ ($x = 0, 0.5, 1.0$) at room temperature, confirm pure single phase with the monoclinic $P2_{1/n}$ space group for all three samples, as indicated in Fig. 2(a). Further, the EDX analysis ensures that these three samples are chemically homogeneous and cation stoichiometry is retained at the target composition, i.e., Pr:Sr:Mg:Ir being very close to the 1:1:1:1 and 1.5:0.5:1:1 ratios for PSMIO and PSMIO1505, respectively, while the undoped PMIO attains a nearly 2:1:1 (Pr:Mg:Ir) ratio within the given accuracy of the measurement. The presence of a superlattice reflection at around $2\theta = 20^\circ$ of the XRD patterns suggests significant Mg/Ir ordering at the B site of these three DP compounds. Although the XRD refinements clearly infer full Mg/Ir chemical order at the B site (see the respective occupancies as indicated in Table I) of two Sr-doped compounds, ∼3–4% Mg/Ir disorder remains evident from the XRD refinement of the undoped Pr_2MgIrO_6 case (see Table I). Lattice parameters, atomic positions, site occupancy, along with the goodness factors for all the three samples are listed in Table I. Due to the large size mismatch between Sr^{2+} (1.44 Å) and Pr^{3+} (1.12 Å), Pr/Sr layered ordering is expected at the A site [24] of the PSMIO sample. As a result, the O-Ir-O bond angles (within a single IrO_6 octahedral unit), sitting closer to the Pr(Sr) layer, would be reduced (increased) with respect to the ideal 90° for perfect cubic symmetry. This brings a higher degree of rotational distortion in the IrO_6 octahedra of PSMIO compared to the other two compounds, as displayed in Figs. 2(d)–2(f) and also tabulated in Table II. So, the effect of the noncubic crystal field, arising from IrO_6 octahedral rotation, would be larger in the case of PSMIO. In addition to this, each Ir ion is acted upon by a local noncubic crystal field in all these compounds due to the presence of three oxygen sites, and consequently, three different Ir-O bond lengths [Figs. 2(d)–2(f)]. The structural distortions often bring complex magnetism in iridates [8,25]. Also, the frustrated equilateral triangular network, usually formed out of B-site cations in cubic double perovskites, is replaced by isosceles triangles in all three samples [see Figs. 2(g)–2(i)]. This shall cause different extents of geometric frustration in these compounds.

B. Local structure from EXAFS

The EXAFS data analysis provides the finest details about the local coordination geometry and local chemical order (the antisite defects) which are complementary to the structural information obtained from the XRD analysis (Rietveld refinement) which only probes long-range coherent structural features. The local antisite disorder in the double

TABLE I. All the samples are refined within a single crystallographic phase. The monoclinic $P2_{1/n}$ space group is taken for all the compositions. (a) Pr_2MgIrO_6(300 K): $a = 5.504(8)$ Å, $b = 5.659(8)$ Å, $c = 7.835(4)$ Å; $\alpha = \gamma = 90°$, $\beta = 89.9901°$. $R_p = 20.0$, $R_{wp} = 19.1$, $R_{\rm exp} = 10.26$, and $\chi^2 = 3.48$. (b) $Pr_{1.5}Sr_{0.5}MgIrO_6$(300 K): $a = 5.538(7)$ Å, $b = 5.610(7)$ Å, $c = 7.851(9)$ Å; $\alpha = \gamma = 90°$, $\beta = 90.0055°$. $R_p = 15.6$, $R_{wp} = 14.4$, $R_{\rm exp} = 7.08$, and $\chi^2 = 4.11$. (c) $PrSrMgIrO_6$(300 K): $a = 5.565(7)$ Å, $b = 5.574(2)$ Å, $c = 7.865(8)$ Å; $\alpha = \gamma = 90°$, $\beta = 90.0212°$ $R_p = 21.0$, $R_{wp} = 19.4$, $R_{\rm exp} = 10.56$, and $\chi^2 = 3.37$.

Sample	Atoms	Occupancy	x	y	z	B ($\times 10^3$ Å^2)
	Pr	1.0	0.4928(6)	0.0516(9)	0.2497(6)	2.3(7)
	Mg1	0.964	0	0	0	0.9(5)
	Ir1	0.036	0	0	0	0.9(5)
	Ir2	0.964	0.5	0.5	0	1.2(1)
Pr_2MgIrO_6	Mg2	0.036	0.5	0.5	0	1.2(1)
	O1	1.0	0.1966(2)	0.2655(5)	0.0497(3)	4.7(6)
	O2	1.0	0.6144(8)	0.4756(4)	0.2561(5)	4.7(6)
	O3	1.0	0.2717(2)	0.7937(7)	0.0552(8)	4.7(6)
	Pr	0.75	0.4961(7)	0.0434(1)	0.2506(5)	1.8(5)
	Sr	0.25	0.4961(7)	0.0434(1)	0.2506(5)	1.8(5)
	Mg	1.0	0	0	0	0.8(2)
$Pr_{1.5}Sr_{0.5}MgIrO_6$	Ir	1.0	0.5	0.5	0	1.5(3)
	O1	1.0	0.2015(2)	0.2479(8)	0.0221(2)	7.2(8)
	O2	1.0	0.5873(0)	0.4669(5)	0.2673(1)	7.2(8)
	O3	1.0	0.2788(5)	0.7952(6)	0.0640(9)	7.2(8)
	Pr	0.5	0.4978(1)	0.0259(9)	0.2504(0)	2.9(4)
	Sr	0.5	0.4978(1)	0.0259(9)	0.2504(0)	2.9(4)
	Mg	1.0	0	0	0	1.2(6)
$PrSrMgIrO_6$	Ir	1.0	0.5	0.5	0	2.3(1)
	O1	1.0	0.2053(8)	0.2602(2)	−0.008	6.6(4)
	O2	1.0	0.5728(0)	0.4745(8)	0.2557(8)	6.6(4)
	O3	1.0	0.3041(8)	0.8097(2)	0.0463(5)	6.6(4)

perovskite structure often largely influences the magnetic response [26–28]. Therefore, to confirm the local coordination around (IrO_6) and also the chemical order (antisite defects) at both the *A* and *B* sites, the Ir L_3-edge EXAFS data (see Fig. 3) has been analyzed in the *R* space in the 1–6 Å region for the two Sr-doped samples, and in the 1–4 Å region for the undoped one [see Figs. 3(a)–3(f)]. Unlike the two Sr-doped compounds, the weak nature of the EXAFS signal of Pr_2MgIrO_6, especially in the 5–6 Å region (fourth shell) of the Fourier transform (FT) data [Fig. 3(d)], restricts us to carry out satisfactory fitting of the FT pattern above the third shell (>4 Å) for this sample. Such a weak signal must be attributed to the larger octahedral tilting distortions of Pr_2MgIrO_6 in contrast to the two doped samples, likely in agreement with the XRD results [see Fig. 2(b) and Table II). We applied a multishell data refinement procedure [29,30] in order to access next-neighbor structural information, relevant to describe the chemical order and antisite defects. The obtained results are summarized in Table III. The EXAFS data analysis confirms almost negligible Mg/Ir chemical disorder (≈3%, 1%, and 0.6% for PMIO, PSMIO1505, and PSMIO, respectively) for all the samples with comparable local interatomic distances with the XRD refinements. These disorder percentages obtained from the EXAFS analysis are very much consistent with the XRD refinements [discussed in Sec. III A and shown in Table I]. EXAFS is more suitable for probing the true nature of local chemical order and is not so suitable for probing bulk order; still the values obtained from the EXAFS analysis are mentioned for the sake of completeness. Further, our analysis suggests that every Ir ion appears to find four Pr and four Sr as nearest-neighbor cations in PSMIO, confirming homogeneous Pr/Sr distribution at the *A* site. On the other hand, each Ir sees eight Pr for Pr_2MgIrO_6, while six Pr/two Sr as nearest-neighbor cations around Ir for $Pr_{1.5}Sr_{0.5}MgIrO_6$, as expected for the desired compositions in the respective cases. It should be noted that in the fitting approximation, we did

TABLE II. Estimation of rotational and tilting distortions of the IrO_6 octahedral unit in the form of deviated bond angles for all three samples.

	Connectivities	Pr_2MgIrO_6	$Pr_{1.5}Sr_{0.5}MgIrO_6$	$PrSrMgIrO_6$
	O1-Ir-O2	88.897°	87.907°	82.067°
Rotational distortion	O1-Ir-O3	90.756°	87.152°	82.892°
	O2-Ir-O3	91.944°	88.038°	89.355°
	Ir-O3-Mg	151.271°	147.071°	147.282°
Tilting distortion	Ir-O2-Mg	143.526°	150.315°	155.361°
	Ir-O1-Mg	152.801°	165.262°	166.902°

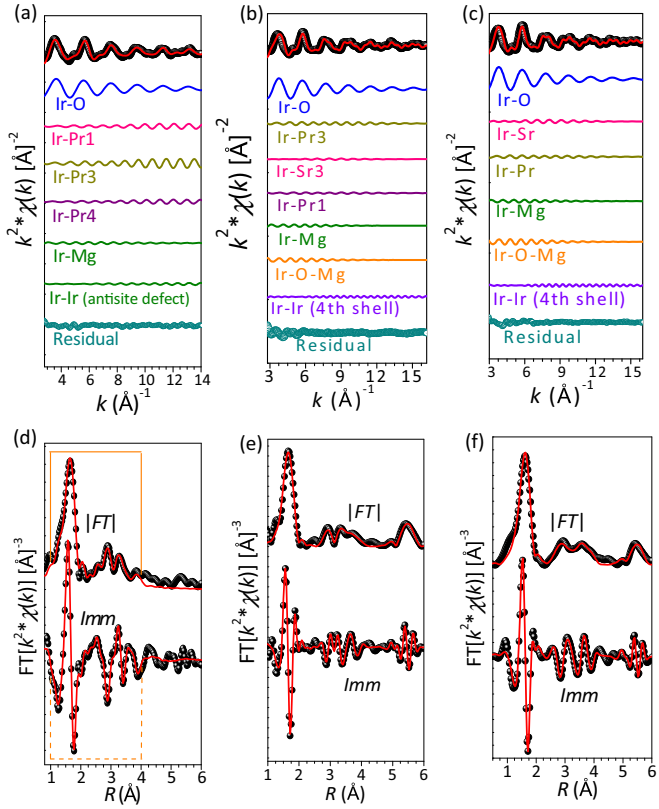

FIG. 3. Ir L_3-edge k^2 weighted experimental EXAFS data (shaded black circles) and the corresponding best fits (red solid line) for Pr_2MgIrO_6 (a) in the k range: 3–14 Å, $Pr_{1.5}Sr_{0.5}MgIrO_6$ (b) in the k range: 3–16 Å, and $PrSrMgIrO_6$ (c) in the k range: 3–16 Å. The contributions from the individual single and multiple scattering paths (solid colored line) and the residual $[k^2\chi_{\rm exp} - k^2\chi_{th}]$ (open cyan dots) are also shown for these three samples, vertically shifted for clarity. The Fourier transforms of the respective experimental data (shaded black circles) and the theoretical (solid red line) curves for Pr_2MgIrO_6 (d), $Pr_{1.5}Sr_{0.5}MgIrO_6$ (e), and $PrSrMgIrO_6$ (f) samples; the magnitude (|FT|) and the imaginary parts (*Imm*) are also indicated; vertically shifted for clarity.

not consider the multiple scattering (MS) contributions for the undoped Pr_2MgIrO_6 sample [see Fig. 3(a) and Table III], as the largely distorted structure and also little higher Mg/Ir disorder reduce the focusing effect, thereby weakening the MS terms and thus, the addition of MS paths did not improve the fitting in this case.

C. Ir-valance state from x-ray absorption near-edge structure (XANES) and core level XPS

The stoichiometric formulas of the $Pr_{2-x}Sr_xMgIrO_6$ ($x = 0, 0.5, 1.0$) samples suggest that Ir should be in the 4+ and 5+ oxidation states in the case of PMIO and PSMIO, respectively, while PSMIO1505 should carry 4.5+ valence (a mixture of 4+ and 5+) of Ir, in order to maintain the charge balance. The Ir-oxidation state has been of central importance in the magnetism of Ir-based compounds, as Ir^{4+}/Ir^{6+} ions are magnetic [1,18,31,32], while Ir^{5+} should ideally be nonmagnetic ($J = 0$) in the jj coupling scenario. So to confirm the charge states, Ir L_3-edge x-ray absorption near-edge structure (XANES) spectra for the three samples have been collected and shown in Fig. 4(a)(i)–4(a)(iii) along with the respective theoretical fittings by fixing the background at the *arctangent* shape and the peak width at 2.5 eV for all three samples. These spectra clearly exhibit a systematic chemical shift [as indicated by the orange dotted line in Fig. 4(a)] as well as the appearance of a rich asymmetric curve shape with Sr doping, indicating a gradual increase of the Ir-oxidation state in these compounds [33,34]. The corresponding second derivative curves, representative of the *white line* ($2p \rightarrow 5d$ transition) feature, are presented in Fig. 4(b). Well-resolved doublet features in the white line spectra of all these compounds indicate the $2p \rightarrow t_{2g}$(low-energy feature) and $2p \rightarrow e_g$ (higher energy peak) transitions. The peak shape as well as a gradual development of the peak feature corresponding to the $2p \rightarrow t_{2g}$ transition, supported further by the enhancement of the area under the solid green curve [shown by the respective XANES spectra fitting in Figs. 4(a)(i)–4(a)(iii)], confirms the expected Ir-oxidation states [33,34] (4+ for $x = 0$ to 5+ for $x = 1.0$ via an intermediate between 4+ and 5+ for $x = 0.5$). On the contrary, the peak shape and the peak intensities [area under each solid blue curve corresponding to the three samples, highlighted in Fig. 4(a)] of the $2p \rightarrow$ empty e_g transition remain nearly unchanged (the minor changes in the peak area are within the error bar of the experiment) irrespective of the change in the Ir-oxidation state in these three compounds. In addition, the shape of the features corresponding to the $2p \rightarrow t_{2g}$ transitions for the three samples [see Fig. 4(b)] matches very well with the observation of previously reported Ir-based double perovskites [33].

In addition, the Ir $4f$ core level XPS spectra were collected and fitted using a single spin-orbit split doublet for the Pr_2MgIrO_6 and $PrSrMgIrO_6$ compounds, while two spin-orbit split doublets were required for the fitting of the 25% Sr-doped compound [see Figs. 4(c)–4(e)]. The energy positions of the respective $4f_{7/2}$and $4f_{5/2}$ features in the doublets along with their spin-orbit separations (around 3.05–3.1 eV) for the three samples, confirm pure 5+ and pure 4+ charge states of Ir in the PSMIO and PMIO compounds, respectively, while mixed 4+/5+ valance states for the 25% Sr-doped sample [7,10,35].

D. Resonant inelastic x-ray scattering (RIXS)

Representative low-resolution Ir L_3-edge RIXS spectra for the three samples (data of both PMIO and PSMIO1505 have been collected from the CLÆSS beamline of ALBA where PSMIO was measured at ESRF) have been plotted after (0,1) normalization as a function of energy loss at $T = 300$ K, shown in Fig. 5(a) in the same panel for the sake of comparison. The largest energy loss features (∼6 eV and ∼9 eV) correspond to charge transfer excitations from the O $2p$ bands to unoccupied Ir t_{2g} and empty e_g bands, respectively [36]. The feature observed at ∼3.5–3.6 eV represents electron excitation from t_{2g} to e_g orbital, indicating the crystal field energies of these samples. The slightly reduced value of $t_{2g} \rightarrow e_g$ crystal field excitation in the PSMIO sample compared to the other two compounds [see Fig. 5(a)] is due to further splitting of the crystal-field-driven Ir t_{2g} and e_g orbitals caused by the IrO_6 octahedral distortion (see Sec. III A). On the other hand, the feature corresponding to O $2p$ to the unoccupied Ir t_{2g}

TABLE III. Local structure parameters as obtained from the EXAFS analysis of the Ir L_3 edge for the three samples. In order to reduce correlation among the parameters, constraints among the parameters were applied, namely, x as the fraction of IrPr pairs, i.e., $N_{\mathrm{IrPr}} = 8x$ and $N_{\mathrm{IrSr}} = 8(1-x)$ for the doped samples, and xx as the fraction of IrOMg configurations, i.e., $N_{\mathrm{IrOMg}} = 6 * xx$ and $N_{\mathrm{IrOIr}} = 6(1-xx)$ for all the samples. The fixed or constrained values are labeled by "∗." The absolute mismatches between the experimental data and the best fit are $R^2 = 0.022$, 0.025, and 0.011 for PSMIO, PSMIO1505, and PMIO, respectively.

Sample	Shell	N	σ^2 ($\times 10^2$ Å^2)	R (Å)
Pr_2MgIrO_6	Ir-O	6.0∗	0.21(4)	2.01(3)
	Ir-Pr1	2.0∗	0.27(3)	3.24(5)
	Ir-Pr3	4.0∗	0.27(3)∗	3.39(3)
	Ir-Pr4	2.0∗	0.27(3)∗	3.51(5)
	Ir-Mg	5.8	0.68(1)	3.86(9)
	Ir-Ir (antisite defect)	0.2	0.68(1)∗	3.86(9)
$Pr_{1.5}Sr_{0.5}MgIrO_6$	Ir-O	6.0∗	0.22(8)	1.98(6)
	Ir-Pr1	2.0∗	0.79(2)∗	3.22(5)
	Ir-Sr3	1.96	0.79(2)	3.41(2)
	Ir-Pr3	4.04	0.79(2)∗	3.41(2)
	Ir-Mg (SS)	5.92	0.74(5)	3.93(8)
	Ir-O-Mg (MS-3 legs)	11.78	0.74(5)∗	4.00(2)
	Ir-Ir (fourth shell)	12.0∗	0.47(5)	5.56(6)
$PrSrMgIrO_6$	Ir-O	6.0∗	0.34(6)	1.95(9)
	Ir-Sr	3.91	0.78(5)	3.34(9)
	Ir-Pr	4.09	0.78(5)	3.32(8)
	Ir-Mg (SS)	5.96	0.56(1)	3.91(4)
	Ir-O-Mg (MS-3 legs)	11.9	0.56(1)∗	3.95(6)
	Ir-Ir (fourth shell)	12.0∗	0.57(5)	5.55(6)

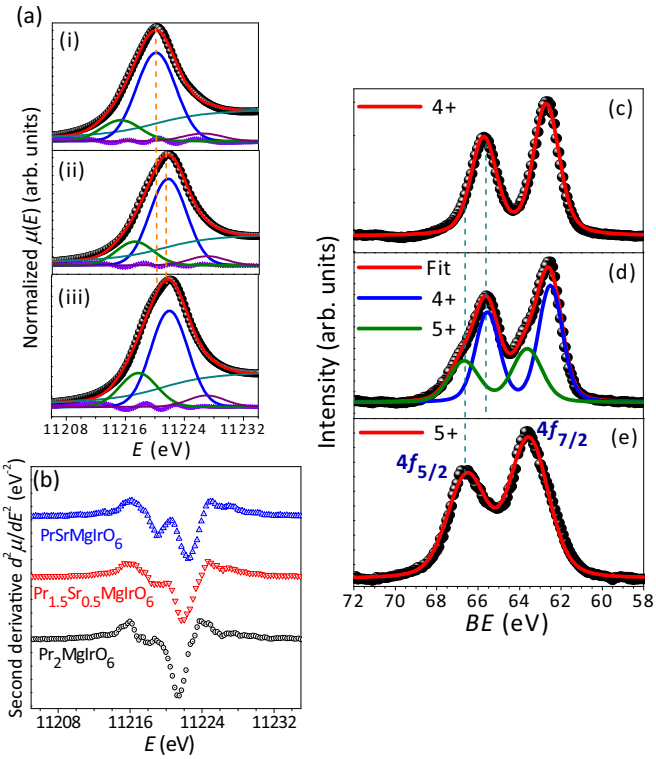

FIG. 4. (a) Ir L_3-edge XANES) spectra (shaded black circles) for Pr_2MgIrO_6 (a)(i), $Pr_{1.5}Sr_{0.5}MgIrO_6$ (a)(ii), and $PrSrMgIrO_6$ (a)(iii), along with their respective fittings (colured solid line). (b) Second derivative curves of the respective normalized absorption spectra, indicating a white line feature. Further, Ir $4f$ core level XPS spectra (shaded black circles) along with the fitting (red solid line) for the Pr_2MgIrO_6 (c), $Pr_{1.5}Sr_{0.5}MgIrO_6$ (d), and $PrSrMgIrO_6$ (e) samples.

transition gets consistently intensified in the doped samples [see Figs. 5(a)–5(c)], as Sr doping introduces Ir^{5+} ($5d^4$) ions which creates a greater number of holes in the t_{2g} orbital, thereby enhancing the transition probability and consequently resulting in a sharp feature at ∼6 eV for the pentavalent iridate DP PSMIO, shown in Fig. 5(a). Although the rising feature (at ∼6 eV) is consistent with the increasing number of Ir t_{2g} holes in these compounds upon Sr doping, the discrepancy in the order of their intensities is possibly due to different experimental setups in ESRF (ID23 beamline for PSMIO) and ALBA (CLÆSS beamline for the other two samples) synchrotron facilities. While the ESRF setup pushes energy resolution at the expense of flux, the opposite is applicable to the ALBA setup. In addition, within a similar measurement configuration the increased intensity of the O $2p$ to Ir e_g transition (at ∼9 eV) in $Pr_{1.5}Sr_{0.5}MgIrO_6$ compared to the undoped Pr_2MgIrO_6 [shown in Figs. 5(b) and 5(c)] further supports a higher degree of IrO_6 octahedral distortions in PSMIO1505 relative to the PMIO case [discussed in Sec. III A and shown in Figs. 2(d) and 2(e)] and also points to the difference in local environments around the Ir-O octahedra due to the existence of mixed Ir^{4+}/Ir^{5+} valence states in PSMIO1505, contrary to the pure 4+ charge state of PMIO. Consequently, the different extent of transition probabilities between the differently splitd Ir energy levels of these two compounds causes intensity variation in the absorption spectra.

E. Electrical resistivity and XPS valance band spectra

The temperature variation of electrical resistivity [($\rho(T)$] for the three samples are shown in Fig. 6. Upon cooling, resistivity increases continuously for all the samples, indicating

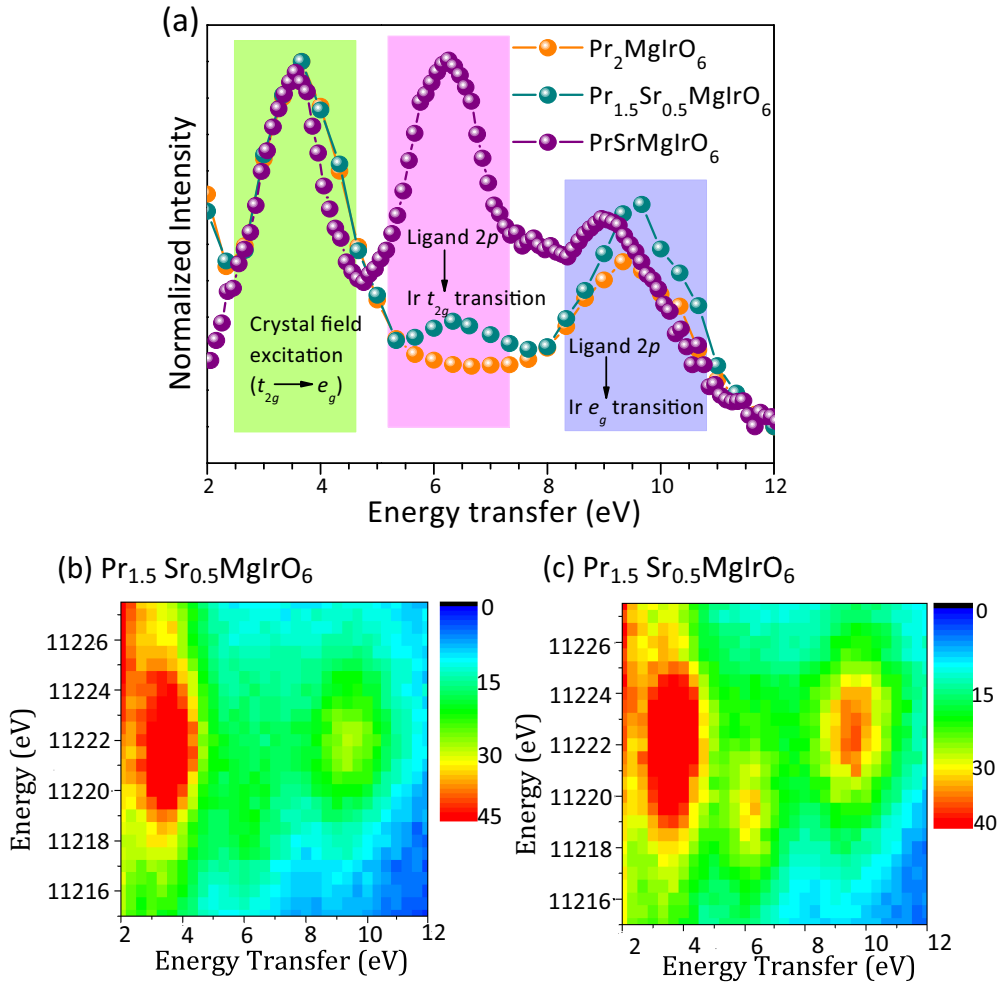

FIG. 5. (a)–(c) Low-resolution high-energy RIXS features for the three samples.

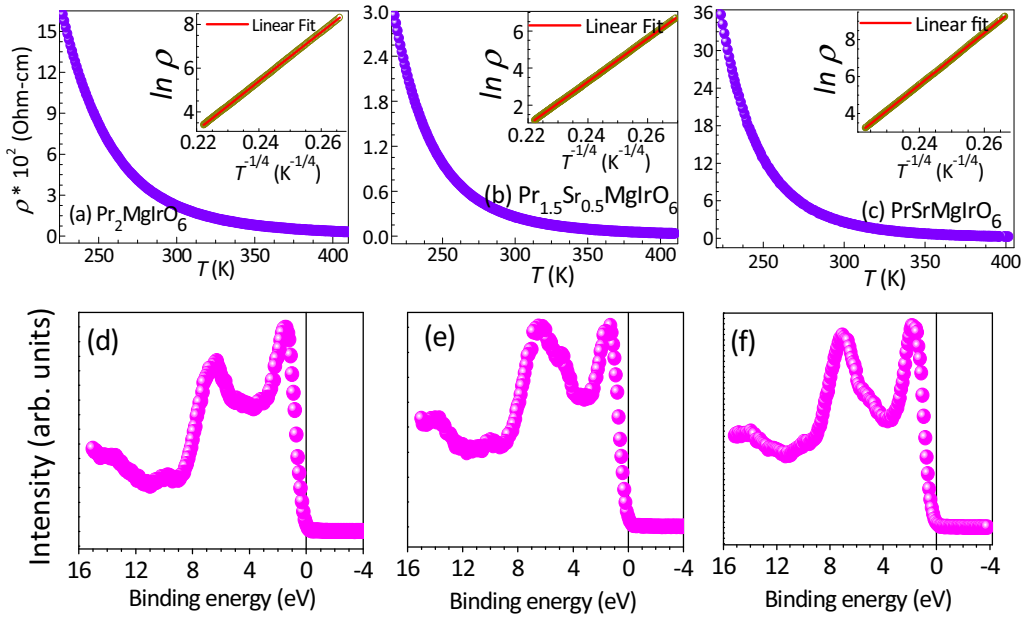

FIG. 6. (a)–(c) Temperature-dependent electrical resistivity variations for the three samples. Inset: Corresponding Mott VRH fitting; further, XPS valance band spectra for the (d) Pr_2MgIrO_6, (e) $Pr_{1.5}Sr_{0.5}MgIrO_6$, and (f) $PrSrMgIrO_6$ samples.

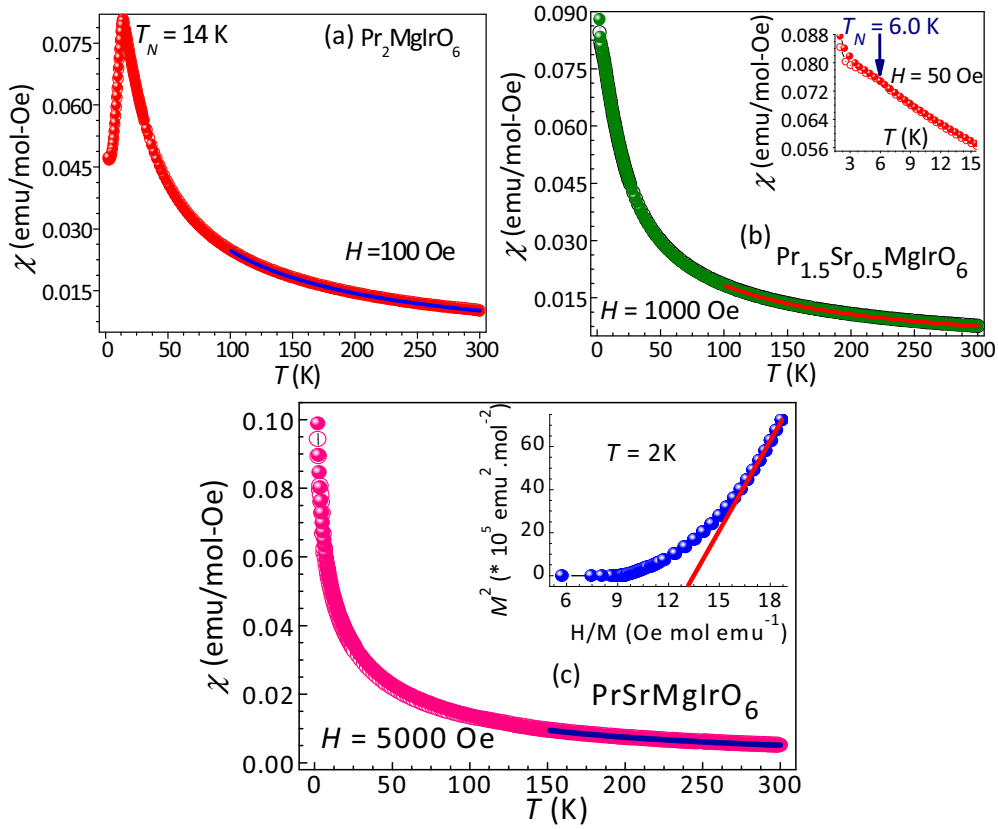

FIG. 7. Zero-field-cooled (open circles) and field-cooled (shaded circles) dc magnetic susceptibilities as a function of temperature [$\chi(T)$] under 100 Oe applied field for Pr_2MgIrO_6 (PMIO) (a). (b) The temperature-dependent dc magnetic susceptibility in both ZFC (open green circles) and FC (shaded green circles) modes at $H = 1000$ Oe field for $Pr_{1.5}Sr_{0.5}MgIrO_6$ (PSMIO1505). Inset: Expanded view of the 50 Oe $\chi(T)$ curve for the same sample. (c) ZFC (open pink circles) and FC (shaded pink circles) dc magnetization curves for the $PrSrMgIrO_6$ (PSMIO) sample at 5000 Oe applied magnetic field. Inset: The Arrot plots (M^2 versus H/M curve) at $T = 2$ K.

insulating behaviors of them. Further, the $\rho(T)$ curves could be modeled by Mott variable range hopping (VRH) mechanism in three dimensions [37] as, $\rho(T) \sim \exp(T_0/T)^{1/4}$, shown in the insets to Figs. 6(a)–6(c)]. The valance band XPS spectra for these three samples were further collected and the results are summarized in Figs. 6(d)–6(f). As displayed, the complete absence of density of states at the Fermi level affirms the charge-gapped electronic ground states for all three compounds. Thus our observation of the insulating nature in all three samples immediately refutes the claim for half-metallicity in the Sr-doped compounds [16], suggesting the dominance of SOC over the exchange splitting, similar to the other reported 5*d* iridate double perovskites [10,19].

F. Magnetization

Next we have investigated the nature of magnetization of these systems. The dc magnetic susceptibility $\chi(T)$ of the undoped PMIO sample [Fig. 7(a)], measured at 100 Oe applied magnetic field, shows sharp AFM transition around 14 K. A Curie-Weiss (C-W) fit [using equation $\chi = \chi_0 + C/(T - \Theta_{CW})$; χ_0 is the temperature-independent paramagnetic susceptibility while C and Θ_{CW} represent the Curie constant and Curie-Weiss temperature, respectively] to the field-cooled susceptibility data [shown by the blue solid line in Fig. 7(a)], in the temperature range 100 K $\leqslant T \leqslant$ 300 K, provides an effective paramagnetic (PM) moment $\mu_{\text{eff}} \sim 5.2\mu_B$/f.u. and a negative $\Theta_{CW} \sim -36.3$ K, suggesting AFM interactions within the compound. In order to understand the contribution of the magnetic Pr^{3+} ion on magnetism and to estimate the spin-orbit-coupled Ir^{4+} moment, we have considered the temperature-dependent dc magnetization of an isostructural Ir-double perovskite La_2MgIrO_6 (LMIO) [18] and we also synthesized the same LMIO compound for a better comparison of the Curie-Weiss analysis between PMIO and LMIO in the same temperature range and applied magnetic field. Due to similar lattice constants of LMIO with PMIO, any change of the Ir-Ir interactions due to lattice change could be presumed to be negligibly small. Further, the same oxidation states of both Pr and La ensures that for both compounds the Ir-oxidation state will remain the same. The AFM transition temperature (~12.5 K) of LMIO [18] resembles the AFM transition of the PMIO. Further, the effective paramagnetic moment, obtained from the Curie-Weiss fit on the field-cooled $\chi(T)$ data of LMIO in the 100–300 K temperature range (not shown in the figure), takes a value of $\sim 1.36\mu_B/Ir^{4+}$. Using this moment value for Ir^{4+} and considering the paramagnetic moment for a Pr^{3+} ion in the *LS* coupling limit to be $3.58\mu_B$ [17,38], the theoretically calculated effective magnetic

moment for PMIO becomes

$$\mu_{\text{eff}} = \sqrt{2(\mu_{\text{eff}})^2_{Pr^{3+}} + (\mu_{\text{eff}})^2_{Ir^{4+}}}\mu_B/\text{f.u.}, \quad (1)$$

$$\Rightarrow \mu_{\text{eff}} = \sqrt{2(3.58)^2 + (1.36)^2}\mu_B/\text{f.u.} = 5.24\mu_B/\text{f.u.} \quad (2)$$

This value is in extremely good agreement with our C-W fit. Actually, Pr^{3+} is a non-Kramer ion, and therefore, sufficiently low symmetry crystal field at the *A* site of the perovskite/double perovskite structure completely removes the degeneracy of the *J* ground multiplet of Pr^{3+} and results in nine singlets [39–42]. As a result of which, Pr^{3+} residing at the *A* site of these perovskite/double perovskite compounds [38–41,43] does not possess any kind of magnetic coupling with the magnetic *B* site. So it should be quite convincing to claim that the ordered magnetic behaviors of all three samples in the present study will solely be influenced by the spin-orbit-coupled Ir moments, while Pr^{3+} should only act as the paramagnetic background over the entire measuring temperature range.

The dc magnetic susceptibility for the 25% Sr-doped sample (PSMIO1505) in a 1000 Oe applied field is presented in Fig. 7(b). The susceptibility curves remain nearly featureless without any ZFC/FC divergence, similar to the observation of most d^4 iridates [9,10,44,45]. Only a very weak AFM-like kink appears at ∼6 K [inset to Fig. 7(b)]. This suggests a weakening of the magnetic interactions. Curie-Weiss fitting on the 1000 Oe field-cooled $\chi(T)$ data in the temperature range 100–300 K provides an effective paramagnetic moment, $\mu_{\text{eff}} \sim 4.5\mu_B$/f.u., and a negative Θ_{CW} of ~ -38.5 K. Considering a nonmagnetic ground state for Ir^{5+}, the theoretically calculated effective magnetic moment for PSMIO1505 would be

$$\mu_{\text{eff}} = \sqrt{1.5(\mu_{\text{eff}})^2_{Pr^{3+}} + 0.5(\mu_{\text{eff}})^2_{Ir^{4+}} + 0.5(\mu_{\text{eff}})^2_{Ir^{5+}}}, \quad (3)$$

$$\Rightarrow \mu_{\text{eff}} \approx \sqrt{1.5(3.58)^2 + 0.5(1.36)^2}\mu_B/\text{f.u.}, \quad (4)$$

$$\Rightarrow \mu_{\text{eff}} = 4.49\mu_B/\text{f.u.} \quad (5)$$

This value again agrees very well with our C-W fitting. Actually, Sr^{2+} doping introduces Ir^{5+} ($5d^4$), which increases the spatial separation between the magnetic Ir^{4+} ions due to increased density of the Ir^{5+} ions upon hole doping. Thus, the strength of the magnetic exchange interaction between the magnetic Ir^{4+} ions is suppressed with respect to the undoped compound, resulting in a weakening of the AFM transition in PSMIO1505. Also the greater extent of exchange frustration within the isosceles Ir triangular network [see Fig. 2(h)] of this compound compared to the undoped one [see Fig. 2(g)] possibly dilutes the effect of the AFM transition in the present case. Like in PMIO, on top of the Ir magnetism, the Pr^{3+} sublattice only enhances the total PM moment of this system.

Finally, the temperature variation of the 5000 Oe dc magnetic susceptibility [$\chi(T)$] curves for the PSMIO sample is presented in Fig. 7(c). The absence of any feature confirms no magnetic long-/short-range ordering down to 2 K, like in other d^4 Ir compounds [9,44]. The C-W fit on the field-cooled data, in the temperature range 150–300 K, gives a Θ_{CW} of ~ -38.6 K. The effective magnetic moment ($\mu_{\text{eff}} \sim 3.89\mu_B$/f.u.), obtained from this fit, is slightly higher than $3.58\mu_B/Pr^{3+}$. So the remaining excess moment ($\sim 0.3\mu_B$) is getting developed obviously at the Ir^{5+} site, driving the system away from the expected $J = 0$ nonmagnetic ground state. The presence of a few percent of magnetic Ir^{4+}/Ir^{6+} ions, as the possible origin of moment development [9,46], could be refuted in the present case from the Ir L_3-edge XANES analysis (discussed in the XANES portion) and also the Ir $4f$ core level XPS data (discussed in the XPS portion). Further, negligible Mg/Ir chemical disorder (<1% as discussed in the EXAFS section) at the *B* site of this DP strongly discards any chance of moment generation due to enhanced Ir-Ir exchanges because of Mg/Ir antisite defects. So one might consider the effect of noncubic crystal field (see structural discussion), which reduces the effect of atomic SOC, as the origin of weak Ir moments [8] in this compound by redistributing the spin-orbit-coupled *J* multiplets. In addition, another highly decisive factor for the development of such small finite moment on individual Ir^{5+} could be due to intersite real Ir-Ir hopping causing delocalization of the intrasite Ir^{5+} holes and thus, deviating from a perfect atomic d^4 configuration [10,15], causing magnetic ground state. According to Nag *et al.* [15], it has been argued that even moderate hopping, present in the systems like cubic Ba_2YIrO_6 [10], can be suspected as the origin of atomic SOC rescaling and subsequent development of finite magnetic moment. The deviation from C-W law below 150 K suggests the development of short-range correlations between the Ir moments [47]. Despite having significant AFM interactions (negative θ_{CW} value), this sample does not possess ordering down to 2 K at least possibly due to geometric frustration arising from the isosceles Ir triangles of three nearly identical Ir-Ir bond distances [see Fig. 2(i)]. Thus, the Ir-Ir AFM exchange interactions are expected to be of nearly similar strength for nearest neighbors on all of the Ir sites in PSMIO, preventing this compound from magnetic order. The field-dependent magnetization $M(H)$ curves for PSMIO (not shown) show neither hysteresis nor any saturation in any of the temperatures. As evident in the inset to Fig. 7(c), the 2 K Arrot plot (M^2 versus H/M) renders an interception on the negative M^2 axis, clearly discarding the presence of spontaneous magnetization vis-a-vis FM components [48] in this PSMIO sample.

G. High-resolution RIXS of PSMIO

Although a nonmagnetic $J = 0$ ground state is ideally expected at the Ir^{5+} site of the PSMIO compound from a single atomic perspective, the presence of a finite magnetic moment on each individual Ir^{5+} ion has been confirmed from magnetization measurements. So, it is important to comment on the trueness of the atomic *J* state description in this double perovskite. Consequently, the high-resolution Ir L_3-edge RIXS spectra (measured at $T = 20$ and 300 K) of the $PrSrMgIrO_6$ sample have been collected and illustrated in Fig. 8(a). During experiment, the incident photon energy was kept fixed at 11.216 keV, which was found to enhance the low-energy inelastic features of the *J* multiplet excitations. In order to gain deeper insight into these features, the high-resolution low-energy RIXS spectra of perfectly *B*-site

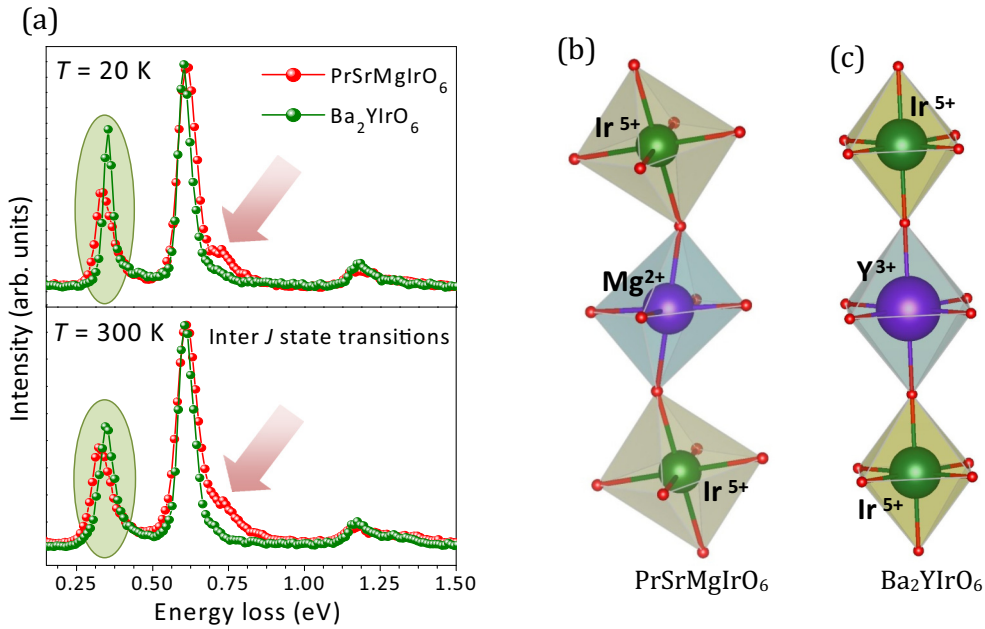

FIG. 8. (a) High-resolution RIXS spectra at $T = 20$ K (upper panel) and 300 K (lower panel) for the $PrSrMgIrO_6$ sample, clearly showing the low-energy inelastic features. Also, the 20 and 300 K low-energy RIXS features for another double perovskite Ba_2YIrO_6 are further plotted in the respective figures for comparison. Ir-Ir hopping pathways for $PrSrMgIrO_6$ (b) and Ba_2YIrO_6 (c) samples, mediated via corner-shared $(Mg/Y)O_6$ octahedral units.

ordered cubic double perovskite Ba_2YIrO_6 were measured within the same technical specifications [10] as PSMIO at $T = 20$ and 300 K, and the subsequent results are represented in Fig. 8(a) along with PSMIO. Like in Ba_2YIrO_6 (BYIO) [10], we observe three similar inelastic peaks below 1.5 eV here in PSMIO. Although the shape and energy positions of these three peaks appear similar in both the samples, subtle changes in these inelastic RIXS features are clearly evident, as demonstrated by intensity enhancement and a shift in energy position of the first feature [indicated by the greenish ellipses of Fig. 8(a)] as well as the development of a prominent shoulder in the higher-energy side of the second peak [shown by red shaded arrows in Fig. 8(a)] in the PSMIO sample contrary to the Ba_2YIrO_6 case. Clearly, both these compounds belong to the double perovskite crystal structure with rocksalt ordered Y-Ir/Mg-Ir arrangements at the B site while the only difference lies in the space group symmetry of the respective crystal structures. It is known that a perfectly cubic $Fm\bar{3}m$ is adopted by BYIO while much lower monoclinic crystal symmetry becomes applicable in PSMIO, and as a result, hopping pathways [see Figs. 8(b) and 8(c)] for PSMIO suffer significant octahedral tilting distortion in terms of Ir-O-Mg bond angles in contrast to 180° Ir-O-Y connectivity for BYIO. On top of it, a monoclinic symmetry-driven local noncubic crystal field around the IrO_6 octahedra of PSMIO removes the Ir t_{2g} degeneracy and consequently rearranges the Ir energy levels, opposite to the ideal cubic crystal field for BYIO [10]. In such a scenario, we may qualitatively infer that the aforementioned differences in RIXS features for $PrSrMgIrO_6$ relative to the Ba_2YIrO_6 should be due to the dissimilar Ir-Ir hopping connectivities [Figs. 8(b) and 8(c)] and also the influence of noncubic crystal distortions in PSMIO. Indeed, both hopping and noncubic crystal field have a strong impact on the effective SOC strength in d^4 Ir systems [15] and therefore, defining the spin-orbit-coupled Ir energy levels from the perspective of the atomic J picture only, as has been the widely accepted scenario until very recently [49], becomes insufficient, as revealed by Nag *et al.* [15] and Revelli *et al.* [50] recently. So it is very clear that precise estimation of the SOC strength on Ir within the atomic limit is not at all a reasonable approach because the low- energy Ir L_3 inelastic RIXS features would be the outcome of intersite hopping, local noncubic crystal distortions, and several other electronic factors. So to elucidate the effective strength of SOC and the resulting new J states [Fig. 8(a)] in PSMIO, further full multiplet calculations will be required which should include all possible electronic and solid state effects.

IV. CONCLUSIONS

In conclusion, we have performed a systematic study of the structural and physical properties of Pr_2MgIrO_6 and its hole-doped counterparts $Pr_{2-x}Sr_xMgIrO_6$ ($x = 0.5, 1.0$) via x-ray diffraction, x-ray absorption fine-structure, high- and low-resolution RIXS, dc magnetization, and electrical resistivity measurements. We find the insulating charge sector of these three compounds confirming a leading role of SOC on the Ir site. However, the effect of atomic SOC is reduced due to the presence of significant noncubic crystal distortion and the ground state magnetism gets affected by hopping among Ir-Ir sites, producing small correlated moments on every Ir site of the d^4 iridate double perovskite $PrSrMgIrO_6$ and hence, causing a breakdown of the ideal atomic $J = 0$ picture. No sign of magnetic ordering was found down to 1.85 K for this d^4 iridate indicating at frustration parameter ($f = \frac{\Theta_{CW}}{T_N}$ with T_N is the lowest measuring temperature here) being >20,

while exchange interactions between the strongly magnetic Ir^{4+} ions of the undoped Pr_2MgIrO_6 compound result in long-range AFM transition at low temperatures. Compared to the undoped one, $Pr_{1.5}Sr_{0.5}MgIrO_6$, with Ir valence in between 4+ and 5+, exhibits weakening of the magnetic exchange interaction due to half substitution of the magnetic Ir^{4+} ions by nonmagnetic Ir^{5+} ions. As a result, the AFM transition is suppressed. On top of this, Pr^{3+} does not take part in the correlated magnetism of either of these compounds; instead, it only acts as a paramagnetic background to enhance the total paramagnetic moment of all these samples.

ACKNOWLEDGMENTS

A.B. thanks CSIR, India and IACS for supporting fellowship. S.R. akcnowledges the Department of Science and Technology (DST) [Project No. WTI/2K15/74] for support. A.B. and S.R. thank Jawaharlal Nehru Centre for Advanced Scientific Research from DST-Synchrotron-Neutron project, for performing experiments at ESRF (Proposal No. HC-2872) and CLÆSS beamline of ALBA (Barcelona, Spain) synchrotron radiation facility. The authors also thank TRC-DST of IACS for providing experimental facilities.

[1] B. J. Kim, H. Jin, S. J. Moon, J. Y. Kim, B. G. Park, C. S. Leem, J. Yu, T. W. Noh, C. Kim, S. J. Oh, J. H. Park, V. Durairaj, G. Cao, and E. Rotenberg, Phys. Rev. Lett. **101**, 076402 (2008).

[2] W. Witczak-Krempa, G. Chen, Y. B. Kim, and L. Balents, Annu. Rev. Condens. Matter Phys. **5**, 57 (2014).

[3] J. G. Rau, E. K.-H. Lee, and H.-Y. Kee, Annu. Rev. Condens. Matter Phys. **7**, 195 (2016).

[4] T. Sato, T. Shirakawa, and S. Yunoki, Phys. Rev. B **91**, 125122 (2015).

[5] S. J. Moon, H. Jin, K. W. Kim, W. S. Choi, Y. S. Lee, J. Yu, G. Cao, A. Sumi, H. Funakubo, C. Bernhard, and T. W. Noh, Phys. Rev. Lett. **101**, 226402 (2008).

[6] G. Chen and L. Balents, Phys. Rev. B **84**, 094420 (2011).

[7] A. Nag, S. Middey, S. Bhowal, S. K. Panda, R. Mathieu, J. C. Orain, F. Bert, P. Mendels, P. G. Freeman, M. Mansson, H. M. Ronnow, M. Telling, P. K. Biswas, D. Sheptyakov, S. D. Kaushik, V. Siruguri, C. Meneghini, D. D. Sarma, I. Dasgupta, and S. Ray, Phys. Rev. Lett. **116**, 097205 (2016).

[8] G. Cao, T. F. Qi, L. Li, J. Terzic, S. J. Yuan, L. E. DeLong, G. Murthy, and R. K. Kaul, Phys. Rev. Lett. **112**, 056402 (2014).

[9] T. Dey, A. Maljuk, D. V. Efremov, O. Kataeva, S. Gass, C. G. F. Blum, F. Steckel, D. Gruner, T. Ritschel, A. U. B. Wolter, J. Geck, C. Hess, K. Koepernik, J. van den Brink, S. Wurmehl, and B. Büchner, Phys. Rev. B **93**, 014434 (2016).

[10] A. Nag, S. Bhowal, A. Chakraborty, M. M. Sala, A. Efimenko, F. Bert, P. K. Biswas, A. D. Hillier, M. Itoh, S. D. Kaushik, V. Siruguri, C. Meneghini, I. Dasgupta, and Sugata Ray, Phys. Rev. B **98**, 014431 (2018).

[11] G. Khaliullin, Phys. Rev. Lett. **111**, 197201 (2013).

[12] G. Chen, L. Balents, and A. P. Schnyder, Phys. Rev. Lett. **102**, 096406 (2009).

[13] T. Dodds, T. P. Choy, and Y. B. Kim, Phys. Rev. B **84**, 104439 (2011).

[14] S. Bhowal, S. Baidya, I. Dasgupta, and T. Saha-Dasgupta, Phys. Rev. B **92**, 121113(R) (2015).

[15] A. Nag, S. Bhowal, M. M. Sala, A. Efimenko, I. Dasgupta, and S. Ray, Phys. Rev. Lett. **123**, 017201 (2019).

[16] M. P. Ghimire, L.-H. Wu, and X. Hu, Phys. Rev. B **93**, 134421 (2016).

[17] S. J. Mugavero III, A. H. Fox, M. D. Smith, and H.-C. zur Loye, J. Solid State Chem. **183**, 465 (2010).

[18] G. Cao, A. Subedi, S. Calder, J.-Q. Yan, J. Yi, Z. Gai, L. Poudel, D. J. Singh, M. D. Lumsden, A. D. Christianson, B. C. Sales, and D. Mandrus, Phys. Rev. B **87**, 155136 (2013).

[19] W. K. Zhu, C.-K. Lu, W. Tong, J. M. Wang, H. D. Zhou, and S. X. Zhang, Phys. Rev. B **91**, 144408 (2015).

[20] J. R. Carvajal, Physica B **192**, 55 (1993).

[21] L. Simonelli, C. Marini, W. Olszewski, M. Avila Perez, N. Ramanan, G. Guilera, V. Cuartero, and K. Klementiev, Cogent Phys. **3**, 1231987 (2016).

[22] M. Newville, J. Synchrotron Radiat. **8**, 322 (2001).

[23] B. Ravel and M. Newville, ATHENA, ARTEMIS, HEPHAESTUS: Data analysis for X-ray absorption spectroscopy using IFEFFIT, J. Synchrotron Radiat. **12**, 537 (2005).

[24] G. King and P. M. Woodward, J. Mater. Chem. **20**, 5785 (2010).

[25] A. Nag, S. Bhowal, F. Bert, A. D. Hillier, M. Itoh, I. Carlomagno, C. Meneghini, T. Sarkar, R. Mathieu, I. Dasgupta, and S. Ray, Phys. Rev. B **97**, 064408 (2018).

[26] A. Bandyopadhyay, S. K. Neogi, A. Paul, C. Meneghini, I. Dasgupta, S. Bandyopadhyay, and S. Ray, Phys. Rev. B **95**, 024432 (2017).

[27] C. Meneghini, S. Ray, F. Liscio, F. Bardelli, S. Mobilio, and D. D. Sarma, Phys. Rev. Lett. **103**, 046403 (2009).

[28] L. Bufaiçal, L. Mendonça Ferreira, R. Lora-Serrano, O. Agüero, I. Torriani, E. Granado, and P. G. Pagliuso, J. Appl. Phys. **103**, 07F716 (2008).

[29] T. Chakraborty, C. Meneghini, A. Nag, and S. Ray, J. Mater. Chem. C **3**, 8127 (2015).

[30] S. Middey, P. Aich, C. Meneghini, K. Mukherjee, E. V. Sampathkumaran, V. Siruguri, P. Mahadevan, and S. Ray, Phys. Rev. B **94**, 184424 (2016).

[31] G. Cao, V. Durairaj, S. Chikara, L. E. DeLong, S. Parkin, and P. Schlottmann, Phys. Rev. B **76**, 100402(R) (2007).

[32] P. Kayser, M. J. Martínez-Lope, J. A. Alonso, M. Retuerto, M. Croft, A. Ignatov, and M. T. Fernández-Díaz, Eur. J. Inorg. Chem. **2014**, 178 (2013).

[33] J.-H. Choy, J. D.-K. Kim, G. Demazeau, and D. Y. Jung, J. Phys. Chem. **98**, 6258 (1994).

[34] J.-H. Choy, J. D.-K. Kim, S.-H. Hwang, G. Demazeau, and D. Y. Jung, J. Am. Chem. Soc. **117**, 8557 (1995).

[35] A. Banerjee, J. Sannigrahi, S. Giri, and S. Majumdar, Phys. Rev. B **96**, 224426 (2017).

[36] K. Ishii, I. Jarrige, M. Yoshida, K. Ikeuchi, J. Mizuki, K. Ohashi, T. Takayama, J. Matsuno, and H. Takagi, Phys. Rev. B **83**, 115121 (2011).

[37] L. Zhang and Z.-J. Tang, Phys. Rev. B **70**, 174306 (2004).
[38] W. R. Gemmill, M. D. Smith, R. Prozorov, and H.-C. zur Loye, Inorg. Chem. **44**, 2639 (2005).
[39] L. D. Tung, Phys. Rev. B **72**, 054414 (2005).
[40] M. Loewenhaupt, Physica B **163**, 479 (1990).
[41] J. Hemberger, M. Brando, R. Wehn, V. Yu. Ivanov, A. A. Mukhin, A. M. Balbashov, and A. Loidl, Phys. Rev. B **69**, 064418 (2004).
[42] V. Dyakonov, F. Bukhanko, V. Kamenev, E. Zubov, S. Baran, T. Jaworska-Gołąb, A. Szytuła, E. Wawrzyńska, B. Penc, R. Duraj, N. Stüsser, M. Arciszewska, W. Dobrowolski, K. Dyakonov, J. Pientosa, O. Manus, A. Nabialek, P. Aleshkevych, R. Puzniak, A. Wisniewski, R. Zuberek, and H. Szymczak, Phys. Rev. B **74**, 024418 (2006).
[43] M. J. Davis, S. J. Mugavero III, K. I. Glab, M. D. Smith, and H.-C. zur Loye, Solid State Sci. **6**, 413 (2004).
[44] L. T. Corredor, G. Aslan-Cansever, M. Sturza, K. Manna, A. Maljuk, S. Gass, T. Dey, A. U. B. Wolter, O. Kataeva, A. Zimmermann, M. Geyer, C. G. F. Blum, S. Wurmehl, and B. Büchner, Phys. Rev. B **95**, 064418 (2017).
[45] M. Bremholm, C. K. Yim, D. Hirai, E. Climent-Pascual, Q. Xu, H. W. Zandbergen, M. N. Ali, and R. J. Cava, J. Mater. Chem. **22**, 16431 (2012).
[46] K. K. Wolff, S. Agrestini, A. Tanaka, M. Jansen, and L. H. Tjeng, Z. Anorg. Allg. Chem. **643**, 2095 (2017).
[47] T. Dey, A. V. Mahajan, P. Khuntia, M. Baenitz, B. Koteswararao, and F. C. Chou, Phys. Rev. B **86**, 140405(R) (2012).
[48] H. Kumar and A. K. Pramanik, J. Magn. Magn. Mater. **409**, 20 (2016).
[49] M. Kusch, V. M. Katukuri, N. A. Bogdanov, B. Büchner, T. Dey, D. V. Efremov, J. E. Hamann-Borrero, B. H. Kim, M. Krisch, A. Maljuk, M. M. Sala, S. Wurmehl, G. Aslan-Cansever, M. Sturza, L. Hozoi, J. van den Brink, and J. Geck, Phys. Rev. B **97**, 064421 (2018).
[50] A. Revelli, M. Moretti Sala G. Monaco, P. Becker, L. Bohatý, M. Hermanns, T. C. Koethe, T. Fröhlich, P. Warzanowski, T. Lorenz, S. V. Streltsov, P. H. M. van Loosdrecht, D. I. Khomskii, J. van den Brink, and M. Grüninger, Sci. Adv. **5**, eaav4020 (2019).